SCIENCE CHINA Materials ARTICLES

mater.scichina.com link.springer.com

Published online 25 May 2021 | https://doi.org/10.1007/s40843-020-1650-2
Sci China Mater 2021, 64(10): 2519–2529

A novel strategy for the fabrication of high-performance nanostructured Ce-Fe-B magnetic materials *via* electron-beam exposure

Liang Zha[1], Cholsong Kim[1], Chao Yun[1], Dong Zhou[2], Wei Li[2], Xiangdong Kong[3], Li Han[3], Wenyun Yang[1], Shunquan Liu[1], Jingzhi Han[1], Changsheng Wang[1], Honglin Du[1], Weixing Xia[4*], Alberto Bollero[5] and Jinbo Yang[1,6,7*]

ABSTRACT **$Ce_2Fe_{14}B$ compound has a great potential to serve as a novel permanent magnet alternative thanks to the abundant and inexpensive rare-earth element (cerium), while its low magnetocrystalline anisotropy and energy product severely restrict its applications. In this work, a novel strategy combining melt-spinning and electron-beam exposure (EBE) aiming for fabricating high-performance Ce-Fe-B magnetic materials is reported to solve the above-mentioned problem. Remarkably, this strategy facilitates developing a suitable grain boundary configuration without using any additional heavy rare-earth element. Under the optimal EBE condition, the maximum energy product ($(BH)_{max}$) of pure Ce-Fe-B alloy is 6.5 MGOe, about four times higher than that obtained after conventional rapid thermal processing method for the same precursor. The enhanced intergranular magnetostatic coupling effect in the EBE sample is validated by mapping the first-order-reversal-curve (FORC) diagrams. The *in-situ* observation of magnetic domain wall motion for Ce-Fe-B alloy using Lorentz transmission electron microscopy reveals that the boundary layers are very effective in pinning the motion of domain walls, leading to the increased coercivity under EBE, and this pinning effect is further verified by micromagnetic simulations. Our results suggest that CeFeB materials using EBE could be a promising candidate after further processing, which could fill the performance "gap" between hexaferrite and Nd-Fe-B-based magnets.**

Keywords: nanoscale magnets, rapid thermal annealing, Ce-Fe-B, magnetic properties, nanocrystalline material

INTRODUCTION

The growing industrial reliance on renewable energy and increasing concern on energy efficiency throughout the complete lifecycle call for clean energy technologies, where rare-earth-based permanent magnets are playing an important role and can serve as wind turbines and the electromobility sector [1]. However, even for the practical rare-earth-based permanent magnets, it is still a great challenge to achieve a high coercivity (H_{cj}) approaching the magneto-crystalline field to meet the requirements for high-performance magnets. The H_{cj} of rare-earth permanent magnets is extremely sensitive to the microstructure in particular the grain size, grain alignment, and grain boundary (GB) configuration: (1) H_{cj} changes with the variation of grain size and keeps at a high level for nanostructured magnets [2–4]; (2) H_{cj} can be enlarged significantly by the alignment of the hard magnetic grains [5–7] and the formation of an adequate GB configuration [8–9]. Usually, nanostructured magnets are obtained through a rapid solidification process, and optimized GB configuration is achieved by conventional furnace an-

[1] State Key Laboratory for Mesoscopic Physics, School of Physics, Peking University, Beijing 100871, China
[2] Functional Materials Research Institute, Central Iron & Steel Research Institute, Beijing 100081, China
[3] Department of Micro-Nano Fabrication Technology, Institute of Electrical Engineering, Chinese Academy of Sciences, Beijing 100190, China
[4] Key Laboratory of Magnetic Materials and Devices, Ningbo Institute of Material Technology and Engineering, Chinese Academy of Sciences, Ningbo 315201, China
[5] Division of Permanent Magnets and Applications, IMDEA Nanoscience, Madrid, Spain
[6] Collaborative Innovation Center of Quantum Matter, Beijing 100871, China
[7] Beijing Key Laboratory for Magnetoelectric Materials and Devices, Beijing 100871, China
[*] Corresponding authors (emails: xiawxing@nimte.ac.cn (Xia W); jbyang@pku.edu.cn (Yang J))

nealing such as composition design, post-annealing, and/or GB diffusion methods [10–14], which all have a low heating rate below 10 K s^{-1}. Inevitably, this low heating rate induces the grain growth and coarsening, resulting in a detrimental effect on permanent magnet performance [15–19]. Here, we report a novel rapid thermal processing (RTP) strategy, electron-beam exposure (EBE) based on a large beam energy, which can lead to extremely high heating rates in low-dimensional systems such as ribbons and films [7,20,21].

Contrary to the conventional furnace annealing strategies, the extremely high heating rate (in the order of 10^3 K s^{-1}) enabled by EBE makes it possible to engineer GB while maintaining a refined microstructure by preventing the undesired grain growth. In our earlier work, we reported that EBE can tailor the microstructure effectively, such as grain sizes, grain shapes, and grain alignments [7,20,21]. This strategy is technically new and has been proved to be extensible to other magnetic materials. The choice of Ce-Fe-B here is based on its competitive permanent magnetic properties and the wide availability of cerium. Cerium is one of the most abundant rare-earth elements obtained as a byproduct from neodymium refining. A successful Ce-Fe-B magnet may alleviate the resource shortage problem of rare-earths [22,23].

The EBE heating rate achieved in this study is about 6000 K s^{-1}, as measured on the ribbon surface by an infrared thermometer [7]. The *in-situ* observation of magnetic domain wall motion under an external magnetic field indicates a strong pinning model of coercive mechanism under such an improved microstructure. This result, combined with mapping the first-order-reversal-curve (FORC) diagrams, shows that the origin of coercivity development is through magnetostatic coupling enhancement. Consequently, the maximum energy product obtained by EBE is higher than that obtained by RTP. It is expected that this new fabrication technology may help achieve the desired microstructure of rare-earth permanent magnetic materials and hence enable efficient and balanced utilization of cerium resources.

EXPERIMENTAL SECTION

Material fabrications

Alloy ingots with nominal compositions of $Ce_{7.2}Fe_{86.6}B_{6.2}$, $Ce_{12.2}Fe_{81.6}B_{6.2}$, and $Ce_{17.2}Fe_{76.6}B_{6.2}$ were prepared by induction melting of 99.9% pure primary materials in a high-purity argon atmosphere. More details about the EBE experimental configuration and the set-up can be found in our earlier study [7]. The ribbon thickness was approximately 20 μm, and the length and width were tailored to 1 cm. The corresponding mass was estimated to be 0.153×10^{-3} g, assuming the density was 7.67 g cm^{-3}. The temperature ramping time and annealing time in this work were set at 0.1 and 1 s, while the accelerating voltage and focus current were set at 10 kV and 165 mA, respectively. For comparison, a conventional RTP was carried out by placing the as-spun ribbons onto a silicon wafer in the chamber equipped with a uniform lamp array that can be accurately controlled and monitored. To obtain a proper nanocrystalline structure, the amorphous ribbons were annealed with various durations in the range of 673–1073 K. The heating rates of RTP and EBE were as high as 30–70 and 3000–6000 K s^{-1}, respectively.

Material characterizations

The annealed ribbons were characterized by X-ray powder diffraction (XRD, Cu-Kα radiation, λ = 1.54187 Å) on a single-crystal silicon substrate. Transmission electron microscopy (TEM, JEM-2100F, Talos F200X) with energy dispersive spectroscopy (EDS) was used to examine the microstructure and phase composition for the melt-spun ribbons. Talos F200X was used for *in-situ* observation of the magnetic domain wall motion with a maximum applied magnetic field of 2.2 T. The high-resolution TEM (HRTEM) samples were prepared by the ion milling technique (Gatan691/695), and the Lorentz TEM (LTEM) samples were prepared by the focused ion beam (FIB, Auriga-Carl Zeiss). Magnetic measurements were performed with a physical property measurement system (PPMS-9) and vibrating sample magnetometer (VSM, Lakeshore8600) at room temperature (RT). The maximum energy product $(BH)_{max}$ at RT was calculated using the density of 7.67 g cm^{-3} and a demagnetization correction ($N \approx 0.977$).

Micromagnetic simulations

Magnetization reversal behaviors in the nanostructured Ce-Fe-B magnetic materials were simulated by a finite element software based on the Landau-Lifshitz-Gilbert-Langevin equations. The models were constructed into a geometry consisting of cubic-shaped grains with sizes of 40–100 nm. For the EBE route, the width of the GB was set as 4 nm. Moreover, for RTP, according to our experimental observations, it was considered that grains touch each other without GB. However, abundant small particles with the size of 8 nm distributed randomly on the interface between grains. The magnetic anisotropy

constant (K_1), saturation magnetization ($\mu_0 M_s$), and exchange stiffness (A) of $Ce_2Fe_{14}B$ phase for all models were 1.5 MJ m^{-3}, 1.0 T, and 5 pJ m^{-1}, respectively [24].

RESULTS AND DISCUSSION

Comparison of the crystallization process, magnetic properties and microstructure between RTP and EBE

Different heating rates were achieved by RTP and EBE. During RTP, the crystallization process of the amorphous state is regulated by the power of the lamp array with a heating rate up to 30–70 K s^{-1}. In the case of EBE, the heating rate and heating energy determining the crystallization process are regulated by varying the accelerating voltage, beam current, and irradiation time. The phase evolution with the heating rate is illustrated in Fig. 1. Firstly, melt spinning is used to obtain an amorphous precursor with a uniform atomic distribution of each element. EBE with a rapid heating rate is used in the next step to irradiate the amorphous precursor with a controllable injection energy. The infiltration depth and exposure area radius of the electrons are several micrometers and millimeters in size, respectively, depending on the choice of accelerating voltage and focus

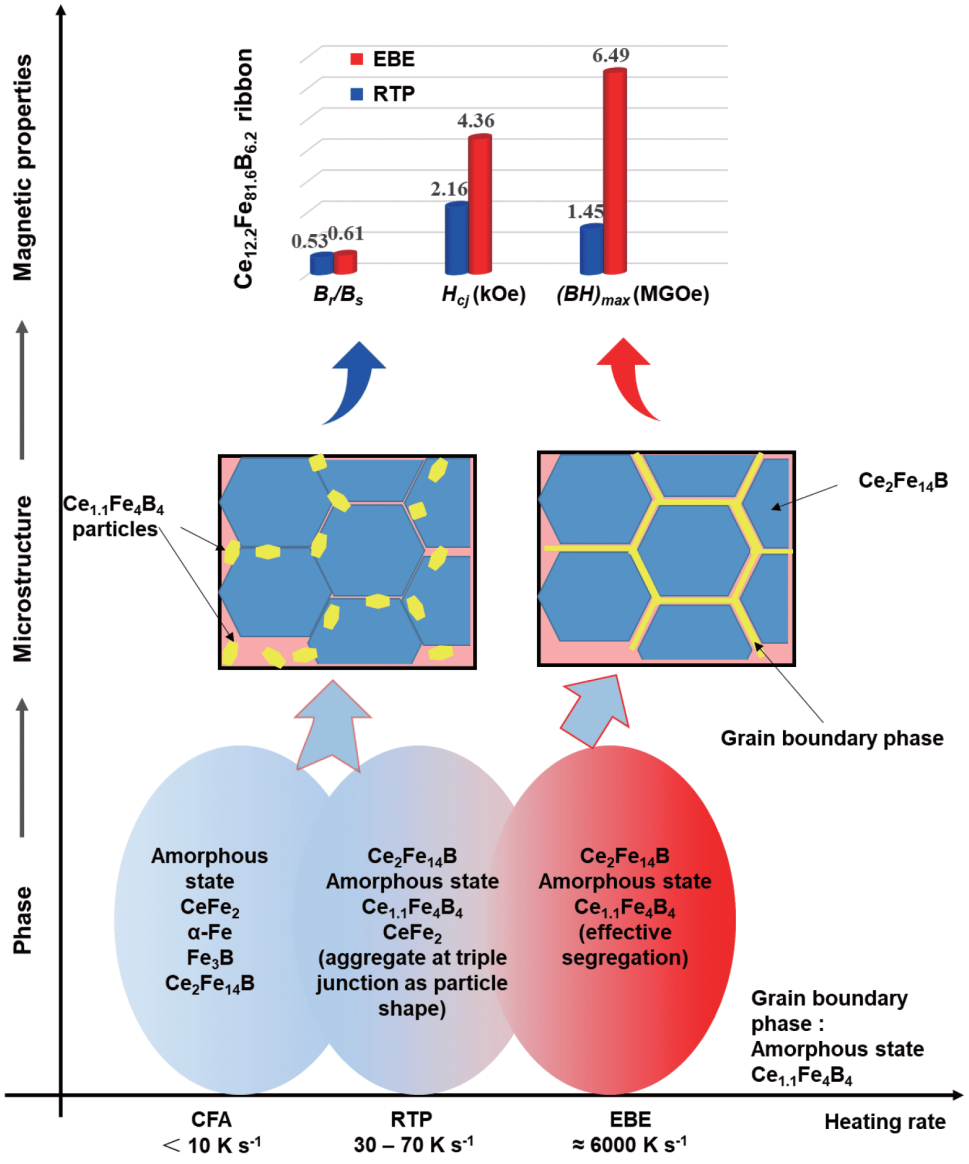

Figure 1 Schematic of the phase evolution with the heating rate.

current. These ranges of infiltration depth and exposure area are adequate to produce the heat required for inducing the crystallization from top to bottom of the ribbons (thickness of 15–30 μm and width of 5–10 mm). This can be verified by the XRD results shown in Figs S1 and S2. The XRD patterns of both the wheel side and free side show the typical 2:14:1 tetragonal structure. However, for $Ce_{17.2}Fe_{76.6}B_{6.2}$ composition, no preferential peaks were observed on the wheel side or free side, which is different from the Pr-Fe-B system reported before. In Pr-Fe-B with Pr-rich composition, instead of forming an undesired Pr-Fe phase, a quasi-texture nanostructure was induced by EBE due to the high wettability of Pr-rich phase when there is an excess of Pr [7]. When Ce is excessive in Ce-Fe-B, a small amount of undesired $CeFe_2$ phase is observed. This phase may facilitate the long sintering process but inhibit the alignment of the Ce-Fe-B grain in the short annealing period due to its high thermal stability and preferential growth [15,18]. For $Ce_{7.2}Fe_{86.6}B_{6.2}$ and $Ce_{12.2}Fe_{81.6}B_{6.2}$, similar results to Pr-Fe-B were obtained, an extra α-iron phase appeared due to the excess of iron, and a single 2:14:1 phase was observed due to the appropriate Ce/Fe ratio. Compared with the highest heating rate of RTP (70 K s^{-1}), the heating rate achieved by EBE in our experiments is in the range of 3000–6000 K s^{-1}. This extremely fast heating rate greatly improves the efficiency of crystallization [25,26]. The amorphous Ce-Fe-B alloy has been crystallized within 1 s under EBE. To the best of our knowledge, this is by far the most effective technique to complete the crystallization process of Ce-based permanent magnetic materials.

The strength of a permanent magnet is characterized by H_{cj}, and $(BH)_{max}$. The theoretical upper limit values of the H_{cj} and $(BH)_{max}$ of $Ce_2Fe_{14}B$ are H_a = 26 kOe and $\frac{1}{4}M_s^2$ = 34 MGOe [27–29], respectively. Fig. 2 shows the second quadrant of the hysteresis loop for the three different Ce-Fe-B compositions under EBE and optimal RTP conditions (Table 1). These values have been chosen on the basis of a systematic study resulting in the evolutions shown in Fig. S8. For reference, beam currents of 0.4–0.8 mA approximately correspond to temperatures of 700–840 K on the sample surface.

As a first observation from Fig. 2, the EBE-treated sample always provides a higher H_{cj} than the RTP-treated sample. Especially for the $Ce_{12.2}Fe_{81.6}B_{6.2}$ composition, both the coercivity and remanence are enhanced significantly. The EBE-treated $Ce_{12.2}Fe_{81.6}B_{6.2}$ composition reaches values as high as H_{cj} = 4.4 kOe and $(BH)_{max}$ = 6.5 MGOe. These results indicate that magnetic properties of Ce-Fe-B alloy not only depend on the specific composition but are strongly influenced by the microstructure, which are in turn affected by the heating rate. By comparing the experimental magnetic properties with the theoretical upper limit values of $Ce_2Fe_{14}B$, plenty of room for improvement of the magnetic properties of Ce-based magnets remains open. The EBE provides a new promising approach to further improving the magnetic performance. The considerable increase in magnetic properties by EBE treatment can be explained with further understanding of the microstructure and magnetic domain configuration. A comparison with the other two samples is shown in the Supplementary information. Results obtained in the other two samples also demonstrate the amelioration effect of EBE for Ce-based materials. It must be admitted that although EBE could be scalable for manufacturing materials such as powders, ribbons, or films, it is not well applicable for the bulk magnets. The challenge for the bulk magnets is the cost-

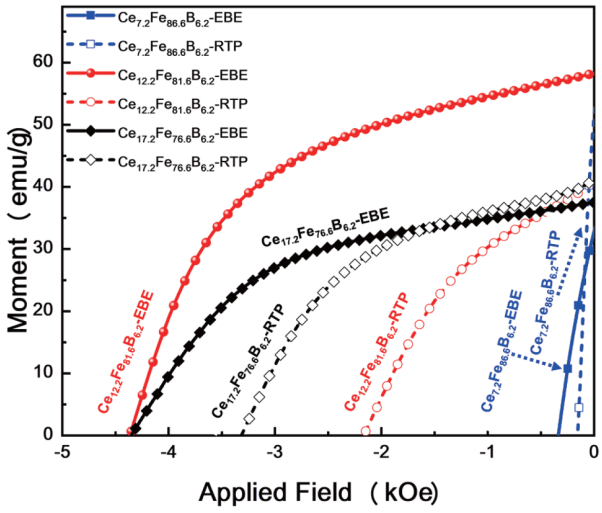

Figure 2 Demagnetization curves of the $Ce_{7.2}Fe_{86.6}B_{6.2}$, $Ce_{12.2}Fe_{81.6}B_{6.2}$, and $Ce_{17.2}Fe_{76.6}B_{6.2}$ ribbons under EBE (full symbols and solid line) and RTP (empty symbols and dashed line).

Table 1 Experimental conditions used by EBE and RTP to achieve and optimized combination of coercivity and remanence in the CeFeB alloys under study

Composition	EBE conditions		RTP conditions	
	Beam current (mA)	Irradiation time (s)	Temperature (K)	Annealing time (s)
$Ce_{7.2}Fe_{86.6}B_{6.2}$	0.8	1	1023	300
$Ce_{12.2}Fe_{81.6}B_{6.2}$	0.4	1	823	300
$Ce_{17.2}Fe_{76.6}B_{6.2}$	0.6	1	823	300

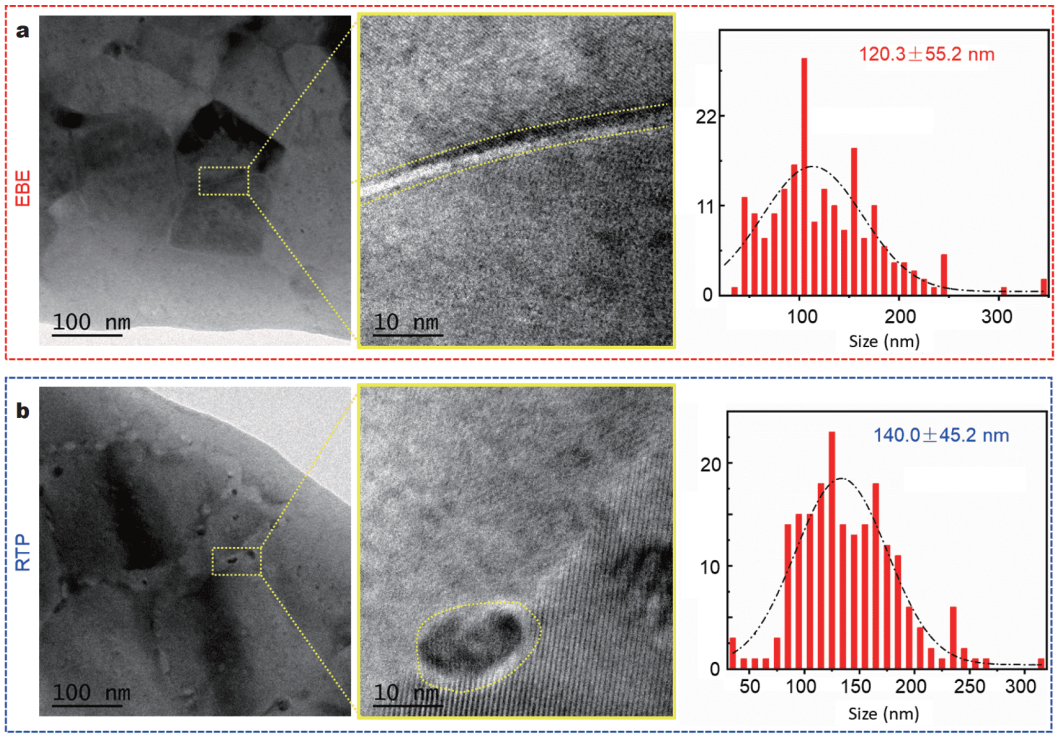

Figure 3 TEM images and the corresponding grain size distributions of $Ce_{12.2}Fe_{81.6}B_{6.2}$ under (a) EBE and (b) RTP.

effective issue, which may be solved by exploring other promising methods for the time being, such as spark plasma and explosive compaction.

Extrinsic magnetic properties are intimately related to the microstructure for permanent magnets. To further understand the relation between the heating rate and the microstructure, we employed the TEM and LTEM techniques to characterize the $Ce_{12.2}Fe_{81.6}B_{6.2}$ composition in detail. As shown in Figs 3 and 4, different microstructures were obtained under RTP and EBE. RTP leads to large-sized hard magnetic grains with few GBs. The grain sizes determined from TEM pictures are 140.0 ± 45.2 nm for RTP and 120.3 ± 55.2 nm for EBE, respectively. A large number of small particles are dispersed randomly along with the GB of the hard-magnetic phase Ce-Fe-B in the sample. Unlike the results obtained on Ce-Fe-B ribbons annealed by conventional furnace [15,16], these small particles (about 8 nm in size) have been identified as $Ce_{1.1}Fe_4B_4$ by high-angle annular dark-field imaging (HAADF) (Fig. 4b) and HRTEM (Fig. 5b) combined with EDS analysis (Fig. S3). $Ce_{1.1}Fe_4B_4$ particles are paramagnetic at RT, which is deleterious to the magnetic properties of the Ce-Fe-B ribbon. The coercivity is sensitive to the grain orientation. If a grain alignment along (00*l*) is formed, the coercivity would be enlarged significantly, as reported in our earlier work about Pr-Fe-B system [7]. We calculate the zone axes of the observed grains as shown in Fig. 5. The zone axes are [276], [$\bar{2}$01] and [10$\bar{1}$] for grains #1, #2 and #4, respectively. No obvious texture is observed; hence the contribution of grain orientation to coercivity in Ce-Fe-B system may not be the major reason of coercivity enhancement in the EBE-

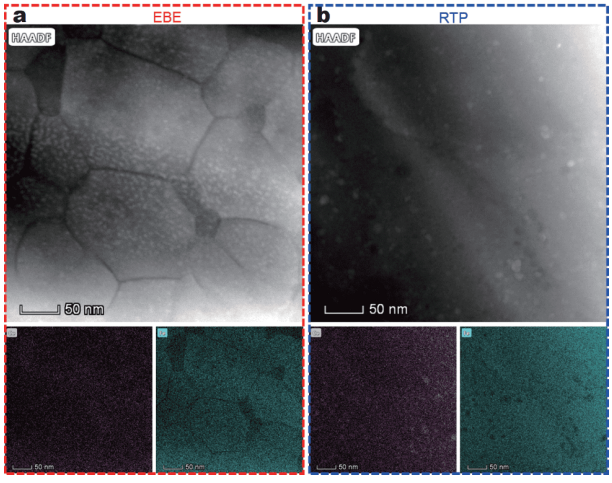

Figure 4 HAADF images of $Ce_{12.2}Fe_{81.6}B_{6.2}$ under (a) EBE and (b) RTP, and the corresponding EDS mappings for Ce and Fe in $Ce_{12.2}Fe_{81.6}B_{6.2}$.

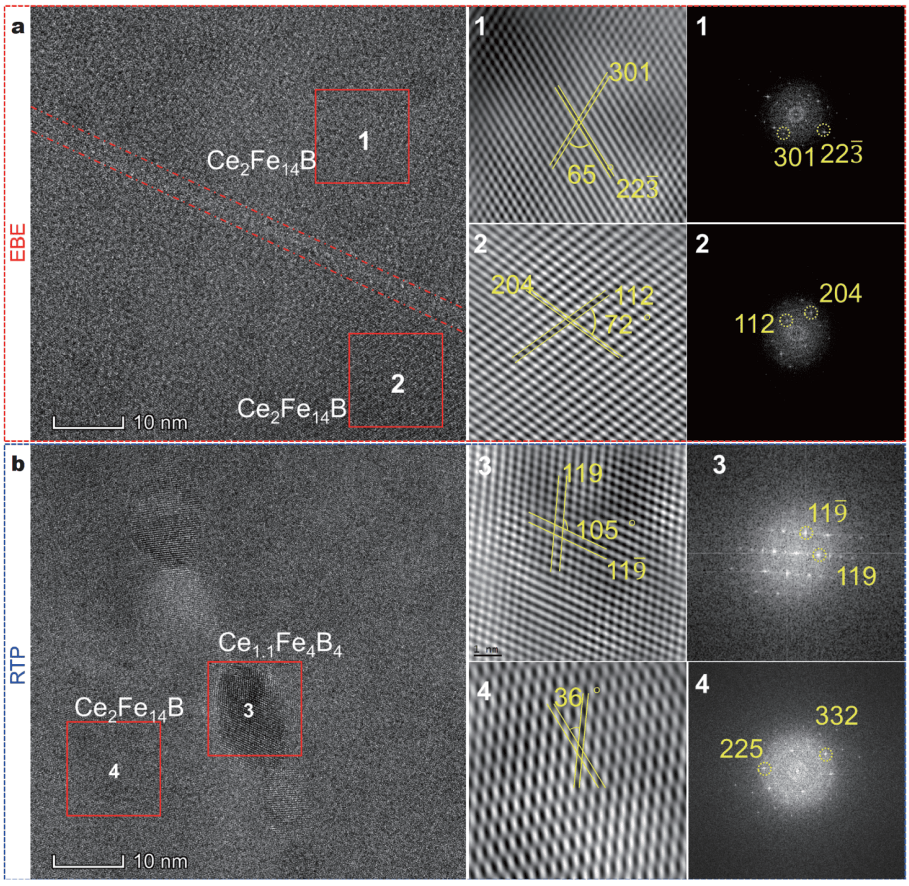

Figure 5 HRTEM images of $Ce_{12.2}Fe_{81.6}B_{6.2}$ under (a) EBE and (b) RTP. #1–#4 are the corresponding high-magnification images and fast Fourier transfor patterns for the selected regions (marked with red squares on the left-hand side images) in (a) and (b).

treated sample. The coercivity is also strongly correlated with the configurations of the RE-rich (RE: rare earth) GB phase, which directly determines the magnetic interaction between neighboring grains [8,30–34]. By comparison with results on the RTP-treated samples, continuous uniform GBs (Fe-lean as shown in Fig. 4a) similar to that observed in high-performance sintered or hot deformed Nd-Fe-B magnets are formed under EBE, with a thickness reaching 2.5 nm (see Figs 3 and 5). This might be one of the main reasons for the improved magnetic response obtained by EBE. The observed GB configuration most likely inhibits the propagation of reversed magnetic domains across grains by improving the intergranular magnetostatic coupling and therefore facilitating the coercivity enhancement in the Ce-Fe-B system [35]. The EBE technique, providing extremely high heating and cooling rates caused by the impingement and collision of thousands of electrons in a fairly short time, is beneficial for achieving the observed GB configuration. Commonly to both techniques, RTP and EBE, the heat energy generated during the process promotes the crystallization from the amorphous state constituting the melt-spun precursor. The significant difference in the heating rate of both techniques is responsible for the difference observed in the crystallite size (coarser with decreasing heating rate). What is more significant, however, is the effect of the heating rate on the induced mobility of the atoms during crystallization and, accordingly, on the resulting GB configuration. When the heating rate is low, as occurring by RTP, a long annealing time is required to complete the crystallization process (300 s). This indicates under RTP condition, Ce travels farther than it does under the EBE condition. Hence the Ce atoms are more likely to form $CeFe_2$ nanocrystal particles with high thermal stability (see Figs 3, 4b, and Fig. S3), enriched at the GBs, thus preventing the formation of a continuous GB phase [36]. When the heating rate increases, according to Fick's law of diffusion [37,38], the diffusion coefficients of the atom will be strengthened, resulting from the ultra-fast energy injection and the quasi-stress

induced by the electron beam irradiation [7]. Thus the crystallization process is significantly accelerated. A delicate balance may be achieved between the competition of crystallization and Ce diffusion under EBE condition, causing the heavier Ce atoms to remain at the GB and form a continuous and uniform GB. This explanation fits well the enhanced coercivity observed in the EBE-processed sample.

Interactions among the magnetic particles and *in-situ* observation of magnetic domain wall motion under EBE and RTP

To further clarify the interactions among the grains with different microstructures (especially different GB configurations) and their correlations with the magnetic properties, FORC was employed to study the coercive mechanism. Talos F200X with a maximum applied field of 2.2 T was used for *in-situ* observation of the dynamic magnetic domain motion during the magnetization and demagnetization processes of the EBE- and RTP-treated ribbons.

An FORC measurement begins with saturating the samples by a sufficiently large positive applied magnetic field, after which the sample is brought to a reversal field, H_a, and then the magnetization is measured as the applied field H increases from H_a back up to saturation. The magnetization at applied field H_b on the FORC with reversal point H_a is denoted by $M(H_a, H_b)$, where $H_b \geq H_a$. The measurement process is repeated for different reversal fields to trace out the FORCs. An FORC distribution is defined as the mixed second derivative:

$$\rho(H_a, H_b) \equiv -\frac{\partial^2 M(H_a, H_b)}{\partial H_a \partial H_b}. \quad (1)$$

The FORC diagram shown here is plotted by the FORCinel program designed by Harrison *et al.* [39], and the smoothing factor is chosen as 3 consistently to make a clear comparison between FORC diagrams while keeping noise to an acceptable level.

When an FORC distribution is plotted by FORCinel, the coordinates are changed from $\{H_a, H_b\}$ to $\{H_u \equiv (H_b - H_a)/2, H_c \equiv (H_b + H_a)/2\}$ to visualize the interactions. After the coordinate transformation, an FORC diagram is a contour of an FORC distribution with H_c and H_u on the horizontal and vertical axes, respectively [40]. According to Pike *et al* [41], H_c is equivalent to the particle coercivity and H_u is equivalent to the local interaction field. As shown in the FORC diagrams (Fig. 6), the vertical spread along the H_u axis is wider in the EBE-treated sample compared with that of the RTP-treated one. This indicates that the magnetostatic coupling is stronger in the EBE-treated ribbon [40,41]. As it is well-known, the GB phase plays an important role in the interactions between the grains [8,9,11,42]. In the EBE-treated ribbon, the GB is well defined, uniform, and continuous as illustrated in Figs 3–5. Hence, the stronger magnetostatic coupling should result from this engineered GB configuration. The role of GB in the magnetostatic coupling was further verified from the dynamic structural changes of the magnetic domain walls observed using *in-situ* LTEM. Fig. S4 shows that most of the magnetic domains in the EBE-treated ribbon are single domains and the domain walls coincide with the GBs. During the initial magneti-

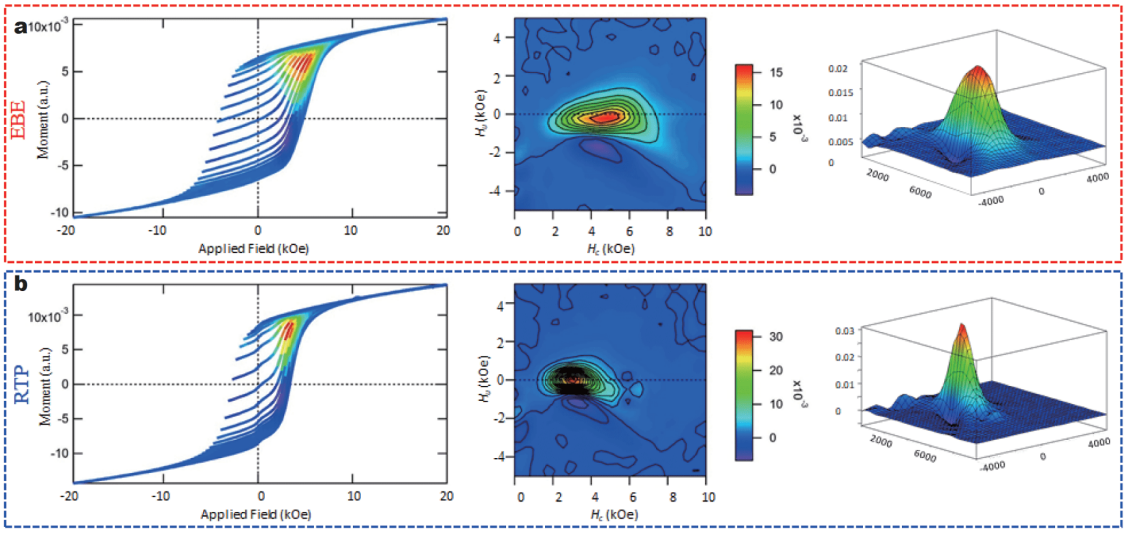

Figure 6 2D and 3D FORC diagrams of the $Ce_{12.2}Fe_{81.6}B_{6.2}$ ribbon under (a) RTP, and (b) EBE. The left columns are the colored FORC curves with the FORC distributions plotted inside the hysteresis loops.

zation process, two typical magnetic domain wall motion models were observed. With increasing magnetic field, the domain wall moves quickly through the grain interior and stays intermittently at the GBs, which directly evidences the pinning effect of the GB, as shown in the Supplementary Video. On the contrary, for the RTP-treated sample, the increase of the magnetic field leads to shrinkage or expansion of the magnetic domain evolving continually from the corner of the domain or the smaller particles. This kind of wall motion is consistent with the nucleation model. This different behavior explains the coercivity enhancement observed in the EBE-treated ribbon. The peak corresponding to the switching field centered at around 4 kOe along the H_c axis for the EBE-treated ribbon is about 2 kOe higher than that determined for the RTP-treated ribbon (Fig. 6), which again is consistent with the coercivity trend. During the demagnetization process *in-situ* observed by LTEM, new domain walls appear more slowly (i.e., need to increase further the external field) in the EBE-treated sample compared with that of the RTP-treated one (see the I, II, and III circles marked in Fig. 7). The image contrast variation for LTEM picture is the reflection of the domain wall motion. In the EBE-treated ribbon, as the magnetic field decreases to 503 mT starting from the saturation magnetization state, a massive image contrast variation occurs. By comparison, this situation occurs at a higher magnetic field of 820.8 mT in the RTP-treated ribbon (more specific magnetic domain wall motion is shown in Figs S5 and S6). This result demonstrates that the activation of the magnetic domain wall motion requires more energy in the EBE-treated sample, in good agreement with the higher coercivity measured for this sample.

This study employs the FORC diagrams combined with the *in-situ* LTEM observation to study the relationship among the microstructure, magnetic grain interactions, and permanent magnet properties in the Ce-Fe-B ternary alloy system. These results reveal that the EBE technique can produce a continuous uniform GB phase in the Ce-Fe-B ternary system, which can isolate magnetic grains effectively, resulting in proper strengthening of the magnetostatic coupling. The obtained results suggest that the GB phase might act as an efficient pinning site of magnetic domains during magnetization reversal, thus increasing the coercivity of the nanostructured Ce-Fe-B ribbon.

Micromagnetic simulations

To provide a more comprehensive insight into the correlation experimentally found between microstructure and magnetic properties, micromagnetic simulations were carried out. The microstructure of the sample prepared under EBE was modeled, as shown in Fig. 8a, which is composed of 125 cubic-shaped grains (40–100 nm) separated by a 4-nm GB (Fe-lean phase) layer. On the other hand, the microstructure of the sample prepared by

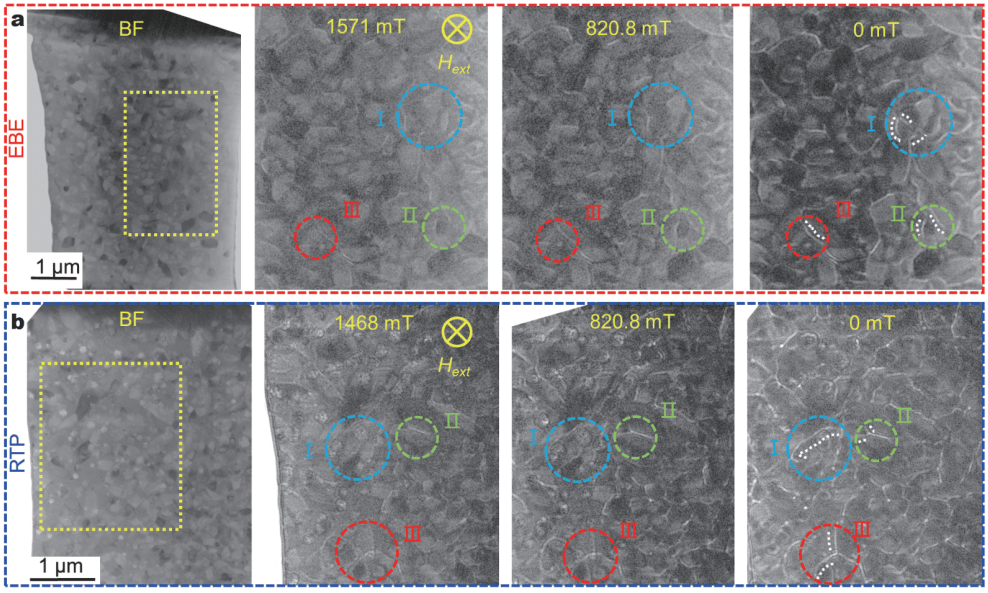

Figure 7 *In-situ* observation of demagnetization process of $Ce_{12.2}Fe_{81.6}B_{6.2}$ ribbon under (a) EBE, and (b) RTP. The white dashed lines in the figures of 0 mT denote the typical magnetic domain wall (more in-detail magnetic domain wall motions are shown in Figs S5 and S6, and the dynamic domain wall motion is shown in Supplementary Video).

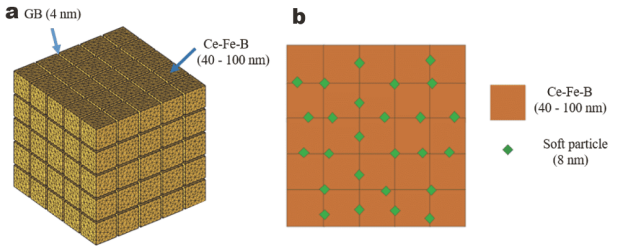

Figure 8 (a) The model for EBE-treated ribbons with cubic-shaped Ce-Fe-B grains (40–100 nm) separated by GB layer (4 nm). (b) The XY section of the bulk model for RTP-treated ribbons with Ce-Fe-B grains (40–100 nm) and soft particles (8 nm).

Table 2 Magnetic parameters of Ce-Fe-B, GB, and soft particles

Materials	K_1 (J m^{-3})	A (J m^{-1})	J_s[a)] (T)
Ce-Fe-B	1.5	5.0	1.17
GB	0	6.0	1.0
Soft particles	0	1.0	1.0

a) J_s is saturation magnetic polarization.

RTP has been simulated by grains (40–100 nm) in close contact with each other with the presence of soft particles with a size of ~8 nm. These soft particles were distributed randomly on the interfaces between Ce-Fe-B grains, as shown in Fig. 8b. The volume ratio that these particles occupy in the system is maintained at 1%. The effective magnetocrystalline anisotropy constant of the soft particles has been assumed to be a negligible value since their magnetization can randomly flip direction under the influence of temperature. The specific magnetic parameters used in micromagnetic modeling are listed in Table 2.

Fig. S7 shows simulation results on magnetization reversal behaviors when the sizes of Ce-Fe-B grain and soft particles are 100 and 8 nm, respectively, and the dependence of the coercivity on the grain size in the simulated Ce-Fe-B system. The result of micromagnetic simulation shows that the coercivity of a Ce-Fe-B magnet with an engineered GB configuration (EBE-type) is about twice higher than that with numerous soft particles and without uniform GB phase (RTP-type). This result supports our previous arguments explaining the differences in the coercivity values obtained using different heating techniques.

The configurations of magnetization reversal simulated for both microstructures (EBE and RTP) are shown in Fig. 9; the size of Ce-Fe-B grain is 100 nm, the thickness of GB phase is 4 nm, and the size of soft particles is 8 nm. In the model of Ce-Fe-B bulk with the engineered GB configuration (EBE-type), nucleation begins at the GB on the surface of the bulk due to the relatively low magnetocrystalline anisotropy, as illustrated in Fig. 9a; $\mu_0 H_n$ (nucleation field) is −0.7 T and $\mu_0 H_c$ (coercive field) is −0.8 T. In the model of bulk Ce-Fe-B with the inclusion of soft particles (RTP-type), nucleation begins at the soft particles with the lower applied field (Fig. 9b), due to their negligible magnetocrystalline anisotropy and low exchange stiffness; $\mu_0 H_n$ is −0.41 T and $\mu_0 H_c$ is −0.49 T.

CONCLUSIONS

This study proposes a new route to developing a high-performance ternary Ce-Fe-B permanent magnet material through a novel strategy that combines melt-spinning for producing amorphous ribbons followed by application of EBE for crystallization of the 2:14:1 structure. The combination of both techniques and, particularly important,

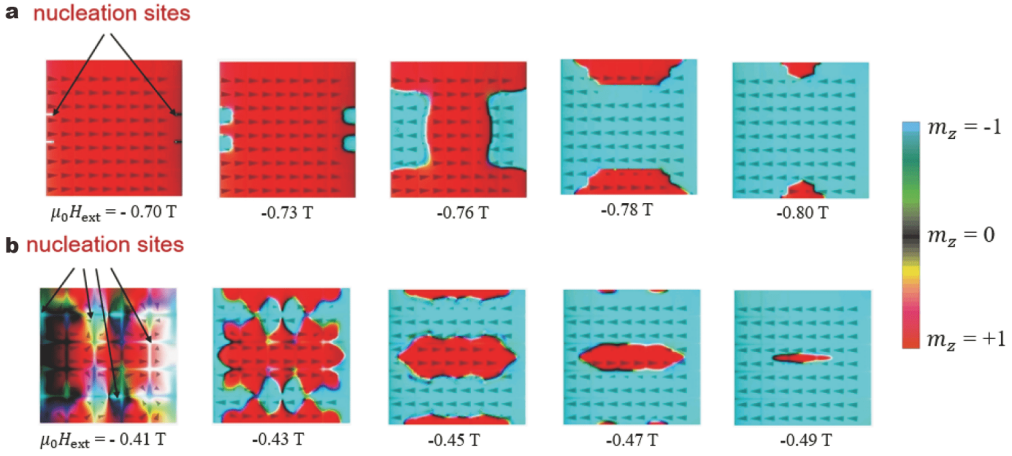

Figure 9 The variation of magnetization and nucleation sites in the models of Ce-Fe-B bulk with (a) an engineered GB configuration (EBE-type), and (b) soft particles (RTP-type) for the Ce-Fe-B grain size of 100 nm, the GB thickness of 4 nm, and the soft particle size of 8 nm.

the use of a high heating rate (about 6000 K s^{-1}) in EBE, allow for a controlled grain growth, a careful design of the GB, and an enhanced intergranular magnetostatic coupling, tunable by controlling the irradiating conditions. Following this route, an optimized composition $Ce_{12.2}Fe_{81.6}B_{6.2}$ shows a coercivity as high as 4.4 kOe and a maximum energy product of 6.5 MGOe. Microstructural and magnetic characterizations, in combination with micromagnetic simulations have proven that the GB is effective in pinning the motion of domain walls, leading to the increased coercivity, which is well above that obtained by other methods using lower heating rates. The conclusions extracted from this study open a new path towards the development of a promising candidate to fill the performance "gap" between hexaferrite and Nd-Fe-B-based magnets.

Received 6 November 2020; accepted 22 February 2021; published online 25 May 2021

1 Gutfleisch O, Willard MA, Brück E, *et al.* Magnetic materials and devices for the 21st century: Stronger, lighter, and more energy efficient. Adv Mater, 2011, 23: 821–842
2 Schrefl T, Fidler J, Kronmüller H. Remanence and coercivity in isotropic nanocrystalline permanent magnets. Phys Rev B, 1994, 49: 6100–6110
3 Manaf A, Buckley RA, Davies HA, *et al.* Enhanced magnetic properties in rapidly solidified Nd-Fe-B based alloys. J Magn Magn Mater, 1991, 101: 360–362
4 Ramesh R, Thomas G, Ma BM. Magnetization reversal in nucleation controlled magnets. II. Effect of grain size and size distribution on intrinsic coercivity of Fe-Nd-B magnets. J Appl Phys, 1988, 64: 6416–6423
5 Lee RW. Hot-pressed neodymium-iron-boron magnets. Appl Phys Lett, 1985, 46: 790–791
6 Pathak AK, Khan M, Gschneidner Jr. KA, *et al.* Cerium: An unlikely replacement of dysprosium in high performance Nd-Fe-B permanent magnets. Adv Mater, 2015, 27: 2663–2667
7 Zha L, Han Y, Pi L, *et al.* Growth of quasi-texture in nanostructured magnets with ultra-high coercivity. Acta Mater, 2020, 195: 282–291
8 Hono K, Sepehri-Amin H. Strategy for high-coercivity Nd-Fe-B magnets. Scripta Mater, 2012, 67: 530–535
9 Kronmüller H, Schrefl T. Interactive and cooperative magnetization processes in hard magnetic materials. J Magn Magn Mater, 1994, 129: 66–78
10 Fidler J, Bernardi J. Transmission electron microscope characterization of cast and hot-worked R-Fe-B:Cu (R = Nd, Pr) permanent magnets. J Appl Phys, 1991, 70: 6456–6458
11 Vial F, Joly F, Nevalainen E, *et al.* Improvement of coercivity of sintered NdFeB permanent magnets by heat treatment. J Magn Magn Mater, 2002, 242-245: 1329–1334
12 Sawatzki S, Kübel C, Ener S, *et al.* Grain boundary diffusion in nanocrystalline Nd-Fe-B permanent magnets with low-melting eutectics. Acta Mater, 2016, 115: 354–363
13 Kim TH, Sasaki TT, Ohkubo T, *et al.* Microstructure and coercivity of grain boundary diffusion processed dy-free and dy-containing Nd–Fe–B sintered magnets. Acta Mater, 2019, 172: 139–149
14 Ma T, Yan M, Wu K, *et al.* Grain boundary restructuring of multi-main-phase Nd-Ce-Fe-B sintered magnets with Nd hydrides. Acta Mater, 2018, 142: 18–28
15 Herbst JF, Meyer MS, Pinkerton FE. Magnetic hardening of $Ce_2Fe_{14}B$. J Appl Phys, 2012, 111: 07A718
16 Zhang ZY, Zhao LZ, Zhong XC, *et al.* Phase precipitation behavior of melt-spun ternary $Ce_2Fe_{14}B$ alloy during rapid quenching and heat treatment. J Magn Magn Mater, 2017, 441: 429–435
17 Jin ZQ, Liu JP. Rapid thermal processing of magnetic materials. J Phys D-Appl Phys, 2006, 39: R227–R244
18 Zhang Y, Ma T, Jin J, *et al.* Effects of $REFe_2$ on microstructure and magnetic properties of Nd-Ce-Fe-B sintered magnets. Acta Mater, 2017, 128: 22–30
19 Zhang JS, Zhao LZ, Liao XF, *et al.* Suppressing the $CeFe_2$ phase formation and improving the coercivity and thermal stability of Ce-Fe-B alloys by Si substitution. Intermetallics, 2019, 107: 75–80
20 Zha L, Wu R, Liu Z, *et al.* Efficiently controlling crystallization and magnetic properties of nanostructured Nd-Ce-Fe-B ribbons *via* electron beam exposure. J Alloys Compd, 2019, 807: 151669
21 Yang J, Han J, Tian H, *et al.* Structural and magnetic properties of nanocomposite Nd-Fe-B prepared by rapid thermal processing. Engineering, 2020, 6: 132–140
22 Cheisson T, Schelter EJ. Rare earth elements: Mendeleev's bane, modern marvels. Science, 2019, 363: 489–493
23 Massari S, Ruberti M. Rare earth elements as critical raw materials: Focus on international markets and future strategies. Resources Policy, 2013, 38: 36–43
24 Liu D, Zhao TY, Li R, *et al.* Micromagnetic simulation of the influence of grain boundary on cerium substituted Nd-Fe-B magnets. AIP Adv, 2017, 7: 056201
25 Chu KT, Jin ZQ, Chakka VM, *et al.* Rapid magnetic hardening by rapid thermal annealing in NdFeB-based nanocomposites. J Phys D-Appl Phys, 2006, 39: 429
26 Tian H, Zhang Y, Han J, *et al.* Synergetic crystallization in a $Nd_2Fe_{14}B$/α-Fe nanocomposite under electron beam exposure conditions. Nanoscale, 2016, 8: 18221–18227
27 Dalmas de Reotier P, Fruchart D, Pontonnier L, *et al.* Structural and magnetic properties of $RE_2Fe_{14}BH(D)_x$; RE=Y, Ce, Er. J Less Common Met, 1987, 129: 133–144
28 Wang T, Medraj M. Intrinsic magnetic properties of $Ce_2(Fe, Co)_{14}B$ and its modifications by Ni and Cu. J Alloys Compd, 2018, 763: 916–925
29 Skoug EJ, Meyer MS, Pinkerton FE, *et al.* Crystal structure and magnetic properties of $Ce_2Fe_{14-x}Co_xB$ alloys. J Alloys Compd, 2013, 574: 552–555
30 Hirota K, Nakamura H, Minowa T, *et al.* Coercivity enhancement by the grain boundary diffusion process to Nd-Fe-B sintered magnets. IEEE Trans Magn, 2006, 42: 2909–2911
31 Akiya T, Liu J, Sepehri-Amin H, *et al.* High-coercivity hot-deformed Nd-Fe-B permanent magnets processed by Nd-Cu eutectic diffusion under expansion constraint. Scripta Mater, 2014, 81: 48–51
32 Sasaki TT, Takada Y, Okazaki H, *et al.* Role of Ga on the high coercivity of Nd-rich Ga-doped Nd-Fe-B sintered magnet. J Alloys Compd, 2019, 790: 750–759
33 Zhang L, Zhu M, Song L, *et al.* The technology and mechanism of coercivity promotion of Ce-rich dual-main-phase sintered magnets. J Magn Magn Mater, 2019, 490: 165414
34 Wang Z, Zhang J, Wang J, *et al.* Coercivity improvement of hot-

deformed Nd-Fe-B magnets by stress-induced Pr-Cu eutectic diffusion. Acta Mater, 2018, 156: 136–145
35 Soderžnik M, Sepehri-Amin H, Sasaki TT, *et al.* Magnetization reversal of exchange-coupled and exchange-decoupled Nd-Fe-B magnets observed by magneto-optical Kerr effect microscopy. Acta Mater, 2017, 135: 68–76
36 Hu H, Peng CJ, Krupanidhi SB. Effect of heating rate on the crystallization behavior of amorphous PZT thin films. Thin Solid Films, 1993, 223: 327–333
37 Serin B, Ellickson RT. Determination of diffusion coefficients. J Chem Phys, 1941, 9: 742–747
38 Allnatt AR, Chadwick AV. Thermal diffusion in crystalline solids. Chem Rev, 1967, 67: 681–705
39 Harrison RJ, Feinberg JM. FORCinel: An improved algorithm for calculating first-order reversal curve distributions using locally weighted regression smoothing. Geochem Geophys Geosyst, 2008, 9: Q05016
40 Roberts AP, Pike CR, Verosub KL. First-order reversal curve diagrams: A new tool for characterizing the magnetic properties of natural samples. J Geophys Res, 2000, 105: 28461–28475
41 Pike CR, Roberts AP, Verosub KL. Characterizing interactions in fine magnetic particle systems using first order reversal curves. J Appl Phys, 1999, 85: 6660–6667
42 Zhu X, Tang X, Pei K, *et al.* Direct observation of magnetization reversal of hot-deformed Nd-Fe-B magnet. AIP Adv, 2018, 8: 015227

Acknowledgements This work was supported by the National Key Research and Development Program of China (2016YFB0700901), the National Natural Science Foundation of China (51731001, 11675006 and 51371009). We appreciate the financial support from the China Scholarship Council (CSC) by a State Scholarship Fund (201906010220). The authors thank Dr. Yanli Li at the Institute of Electrical Engineering (Chinese Academy of Sciences, Beijing, China) for experimental guidance, M.S. Meiling Zhang at the Central Iron & Steel Research Institute (Beijing, China) for aiding in the TEM characterizations, M.S. Jin Zhu for TEM sample preparing. Alberto Bollero acknowledges support from the "Severo Ochoa" Programme for Centres of Excellence in R&D (MINECO, SEV-2016-0686).

Author contributions Zha L designed and performed the experiments, and wrote the paper; Kim C completed the micromagnetic simulation; Xia W and Yang J supervised this study. All authors contributed to the general discussion and revision of the manuscript.

Conflict of interest The authors declare that they have no conflict of interest.

Supplementary information Experimental details and supporting data are available in the online version of the paper.

Liang Zha received his Bachelor's degree from Anhui University in 2016. Currently, he is a PhD candidate at Peking University (PKU). His current research interest focuses on the synthesis and design of functional magnetic materials.

Jinbo Yang is a professor and the leader of the Center for Magnetism Magnetics at the School of Physics, PKU. He received his PhD in condensed matter physics from PKU in 1998 and performed post-doctoral research at the Leibniz Institute for Solid State and Materials Research-Dresden Germany from 1998 to 2000. He then worked at the University of Missouri-Rolla (UMR) from 2001 to 2008. He became a full professor at PKU in 2008. His research interest focuses on the structure and magnetism in condensed matter, including hard/soft magnets, crystal, magnetic and electronic structures of magnetic materials, nanomagnetism and spintronics.

一种通过电子束曝光制备高性能纳米结构Ce-Fe-B磁性材料的新方法

查亮[1], 金哲星[1], 贠超[1], 周栋[2], 李卫[2], 孔祥东[3], 韩立[3], 杨文云[1], 刘顺荃[1], 韩景智[1], 王常生[1], 杜红林[1], 夏卫星[4*], Alberto Bollero[5], 杨金波[1,6,7*]

摘要 $Ce_2Fe_{14}B$作为一种基于广泛而廉价的稀土(铈)的新型永磁体, 低矫顽力和低最大磁能积严重限制了其在永磁领域中的应用. 在这项工作中, 我们报道了一种将熔融纺丝技术和电子束曝光(EBE)技术结合的新方法, 旨在制造高性能Ce-Fe-B磁体. 值得注意的是, 该方法可以在不使用任何其他重稀土元素的情况下调控出合适的晶界构型. 在最佳EBE条件下, 纯Ce-Fe-B合金的最大磁能积为6.5 MGOe, 比常规快速热处理方法制备的合金的最大磁能积高四倍左右. 这说明, 使用EBE制备的CeFeB材料作为前驱体, 经过进一步加工之后, 如热变形或烧结, 有望填补六角铁氧体与Nd-Fe-B磁体之间的市场空白.

